Where Quantum and Fluids entangle

Quantum Computational Fluid Dynamics

Core Benchmark CFD Set

Project number 101080085

Call:	HORIZON-CL4-2021-DIGITAL-EMERGING-02
Topic:	HORIZON-CL4-2021-DIGITAL-EMERGING-02-10
Type of action:	HORIZON Research and Innovation Actions
Granting authority:	European Commission-EU
Project starting date: fixed date:	1 November 2022
Project end date:	31 October 2026
EU-Project duration:	48 months
Project Coordinator:	University of Hamburg (UHH)
Work Package Leader	Technical University of Hamburg (TUHH)
Cooperations	ENGYS (ENG), University of Hamburg (UHH)
Deliverable number:	D2.1
WP contributing to the deliverable:	WP#2 Industry Involvement
Deliverable Type:	Data
Revision:	0
Dissemination level:	Public
Due Submission date:	30.04.2024
Prepared By:	TUHH, ENG, UHH
Internal Reviewers:	TR, EdV, DJ, PO, SB
Final Approval:	

This project receives funding from the European Union's Horizon 2020 HORIZON Research and Innovation Actions Program under Grant Agreement #101080085

Revision History

Version	Date	Who	Changes
V0.0	23.04.2026	TR, EdV, DJ, PO, SB	Creation and publication of the deliverable

This project receives funding from the European Union's Horizon 2020 HORIZON Research and Innovation Actions Program under Grant Agreement #101080085

List of abbreviations

Acronym / Short Name	Meaning
BEV	Battery Electric Vehicle
CA	Consortium Agreement
CFD	Computational Fluid Dynamics
CFL	Courant-Friedrichs-Levy criteria
D	Deliverable
DMP	Data Management Plan
DOI	Digital Object Identifier
EC	European Commission
ENG	ENGYS SRL
EU	European Union
FD	Finite Difference
FDR	Research Data Repository
FV	Finite Volume
FZJ	Jülich Research Centre
KPI	Key Performance Indicator
LES	Large-Eddy Simulation
MPS	Matrix Product States
NSE	Navier Stokes Equations
PlanQC	PlanQC GMBH
PO	Project Officer
QCFD	Quantum Computational Fluid Dynamics
RANS	Reynolds Averaged Navier Stokes
VQA	Variational Quantum Algorithm
TR	Technical Readiness
TUHH	Technical University of Hamburg
TUC	Technical University of Crete
TUM	Technical University of Munich
UHH	University of Hamburg
WP	Work Package
WPL	Work Package Leader

This project receives funding from the European Union's Horizon 2020 HORIZON Research and Innovation Actions Program under Grant Agreement #101080085

Executive Summary

The Quantum Computational Fluid Dynamics (QCFD) project is dedicated to advance quantum computing for Computational Fluid Dynamics (CFD) simulations and their use in industry.

The deliverable D2.1 provides input to the work packages 3, 4, 5, 6, and 7 as part of Work Package 2 (WP2) ("Industry involvement"). This comprises a set of both fundamental and advanced CFD benchmarks, along with initial application-oriented examples and their solutions using conventional CFD methods, some of which are complemented by additional quantum-based approaches.

In accordance with the Data Management Plan (DMP), D2.1 follows the FAIR data principles – Findability, Accessibility, Interoperability, and Reusability – the associated datasets are provided with a detailed metadata structure, unique identifiers, and the corresponding documentation. This ensures that the data is easily accessible and usable by third parties. Public access is granted via a dedicated research data repository (FDR) hosted at the University of Hamburg (UHH), www.fdr.uni-hamburg.de/communities/qcfd/. To make it easier for users to find the data, all datasets belonging to the project are collected in a QCFD community group on the mentioned data server.

This project receives funding from the European Union's Horizon 2020 HORIZON Research and Innovation Actions Programme under Grant Agreement #101080085

Contents

This project receives funding from the European Union's Horizon 2020 HORIZON Research and Innovation Actions Programme under Grant Agreement #101080085

1 Introduction

The use of digital computation has turned Computational Fluid Dynamics (CFD) into an essential tool in nowadays engineering. Innovations in computer science and engineering aim to resolve ever smaller spatial and temporal scales in order to advance the in-depth analysis of the respective problem. This leads to a non-linear increase in computational requirements, i.e., floating-point operations per unit of time and storage capacity. Since the progress of classic hardware in further reducing transistor size and thereby achieving higher computing power is slowing down significantly, it is assumed that there is a limit to the performance increase of classic hardware. Therefore, a paradigm change in computational strategies is needed. To this end, quantum computers offer computational resources beyond any classical performance while maintaining energy efficiency.

To bridge the gap between quantum mechanics and CFD and to supply references to novel algorithms solving engineering problems on current noise intermediate-scale quantum (NISQ) hardware and future fault-tolerant devices, deliverable D2.1 selects case studies to provide CFD data obtained from classical grid-based CFD methods as a benchmark for quantum CFD algorithms.

It is important to understand that quantum algorithms are in their infancy and face significant challenges when it comes to exploiting hardware advantages in technical flows. Therefore, the limitations on the Technical Readiness (TR)-level, the algorithms, and the developing hardware are considered when creating the test cases for quantum CFD, which represents the state-of-the-art at the time the deliverable D2.1 was created. In general, quantum computing-based approaches remain in computational terms very expensive due to current hardware limitations. As a result, coarse spatial resolutions have been adopted for the development of the associated algorithms and their benchmarking. Consequently, the applications presented here are not complex when compared to well-established classical CFD since the algorithms are designed to be applied to the available quantum (emulating) hardware. Thus, terms such as “advanced” or “complex” should be understood in a relative sense, and D2.1 is designed to reflect what is currently possible with quantum methods when applied to CFD problems.

In contrast, higher resolutions can be achieved using quantum-inspired methods, such as Matrix Product State (MPS) techniques, without necessarily relying on quantum hardware. Another case where higher resolution and multi-dimensions are possible is the application of fault-tolerant algorithms that often rely on time-evolution schemes and are in principle more robust, allowing the treatment of larger systems. The cases documented in D2.1 are intended to support all of these quantum computing applications, highlighting the project’s multidirectional research strategy. In the ideal scenario in which the QCFD project could address complex multiphysics problems, such as those encountered in the design of battery electric vehicles (BEVs), a representative case for its benchmarking has already been included.

Given the close connection between quantum algorithms and analogous classical CFD algorithms, the consortium believes it is essential to compare quantum results with classical techniques regardless of numerical resolution.

As already mentioned, challenges related to scalable quantum algorithms, as well as limitations in quantum hardware and its emulation, restrict both the achievable resolution and the level of complexity for the developed methods. For this reason, a direct comparison between the performance of quantum and classical algorithms is not considered meaningful at this point of the project, also because quantum algorithms are still incomplete, largely unoptimized, and in an early stage of maturity. In addition, any potential quantum advantage is expected to emerge at larger scales. Accordingly, the objective of D2.1 is not to benchmark quantum advantage, but rather to support the development of quantum algorithms. The presented data should serve as a basis for assessing methodological differences, without providing insight into quantum hardware performance.

Detailed, dataset-specific documentation is provided to facilitate interpretation and clarify the usability of the data. Each dataset is supplemented with metadata, including parameters, software versions, library dependencies, and simulation time frames. Furthermore, the datasets are classified through a keyword-based search system that incorporates Digital Object Identifiers (DOIs). Through this documentation approach, we aim to ensure the reproducibility of our methods, while enhancing accessibility for both scientific and industrial research. In accordance with the defined Data Management strategy,

This project receives funding from the European Union’s Horizon 2020 HORIZON Research and Innovation Actions Programme under Grant Agreement #101080085

the complete dataset is made available in a dedicated research data repository (FDR) hosted by the University of Hamburg (UHH): www.fdr.uni-hamburg.de/communities/qcfd/, and it is associated with the QCFD project community.

This project receives funding from the European Union's Horizon 2020 HORIZON Research and Innovation Actions Programme under Grant Agreement #101080085

2 Data Description

Deliverable 2.1 is built on the foundation of D1.1 [1] to benchmark newly developed QCFD methods and provides a dataset obtained from classical CFD applications, including mesh-based Finite Difference (FD) or Finite Volume (FV) simulation methods. Where available, quantum results obtained within the project, i.e., together with publications, will be listed as additional datasets. Only examples from structured grids are considered, distinguishing between (a) the spatial dimension of the problem, (b) the time dependence of the problem, (c) the number of (coupled) equations – i.e., the single-/multi-physics approach, (d) the non-/linearity of the underlying equation, (e) the influence of turbulence, (f) the available number of different resolutions/grids, (g) the scientific and industrial relevance, (h) the availability of quantum results, and (i) the specific focus of the respective case.

The remainder of this section provides information on the data processing pipeline, quality and accuracy requirements, as well as the suggested performance indicators (e.g., fail/pass criteria; see Section 2.2).

2.1 Accuracy

Accurate data is fundamental to effective and reliable benchmarking, and is therefore a key component of deliverable D2.1. The standards used are given below:

- List of file formats with the corresponding accuracy, accessible without compression
  - python-numpy std file format (*npy)
  - hierarchical data format version 5 (*hdf5)
  - openFOAM std file format (*foam)
  - ...
- Double-precision floating-point number format
- For complex numbers, the 53-bit significant precision of 16 decimal digits is divided between real and imaginary parts.

2.2 Assessment Criteria

- Absolute error: measure of the deviation between two paired variables.
- L2 (or Euclidean) norm: in general, a norm consists of a function mapping from a vector space to a non-negative real number. In particular, the L2-norm is defined as the square root of the scalar product of a vector with itself.
- Fidelity: often understood as a similarity measure and formed by the scalar product of two normalized vectors.
- Trace distance: a measure of how distinguishable two quantum states are. For pure quantum states, the trace distance is defined as the square root of one minus the fidelity.

This project receives funding from the European Union's Horizon 2020 HORIZON Research and Innovation Actions Programme under Grant Agreement #101080085

3 Cases

This section presents the benchmark cases included in D2.1. They were selected to represent different research strands of the QCFD project, while also drawing on industrial applications. To this end, WP2's first task involves a hierarchical iteration between industry partners and quantum experts to determine key performance indicators (KPIs) for identifying useful benchmark test cases. Based on the KPI-based analysis, multiple test cases have been identified which are organized into three main categories based on their spatial dimensionality, i.e., 1D cases, 2D problems, and 3D applications. Each category is further subdivided into subsections containing individual benchmarks that are identified by a unique DOI.

From a thermofluid dynamic point of view, the benchmark cases are characterized by non-dimensional parameters, viz.

- Reynolds number $Re = \frac{u\,L}{\nu} = \frac{\text{inertial force}}{\text{viscous force}}$ with characteristic velocity $u\,[m/s]$, characteristic length $L\,[m]$, and kinematic viscosity $\nu\,[m^2/s]$
- Nusselt number $Nu = \frac{h\,L}{k} = \frac{\text{convective heat transfer}}{\text{conductive heat transfer}}$ with heat transfer coefficient $h\,[W/(m^2K)]$, characteristic length $L\,[m]$, and thermal conductivity $k\,[W/(mK)]$
- Peclet number $Pe = \frac{u\,L}{\nu} = \frac{\text{advection transport}}{\text{diffusive transport}}$ with characteristic velocity $u\,[m/s]$, characteristic length $L\,[m]$, and kinematic diffusivity $\nu\,[m^2/s]$
- Rayleigh number $Ra = \frac{(\Delta T/T)\,l^3\,g}{\nu\,\alpha} = \frac{\text{time scale of diffusive thermal transport}}{\text{time scale of convective thermal transport}}$ with kinematic viscosity $\nu\,[m^2/s]$, thermal diffusivity $\alpha\,[m^2/s]$, temperature difference $\Delta T\,[K]$, gravitational acceleration $g\,[m/s^2]$, distance $l\,[m]$, and temperature $T\,[K]$

3.1 1D Cases

This first category includes steady and transient heat conduction problems. These cases are well-established 1D examples usually governed by a single differential equation and solved using FD methods. To limit the hardware effort and ensure reproducibility on current quantum devices, relatively coarse discretizations are used.

A detailed description of the corresponding numerical experiments is provided below. As the algorithmic framework is the focal point of the one-dimensional cases, a grid sensitivity study is omitted. Table 1 summarizes the characteristics of the 1D test cases, including a brief description of their main focus and engineering relevance. The key aspects include (1) boundary conditions, (2) technically more relvant inhomogeneous material, and (3) transient behavior. The governing equations comprise diffusion (D), and unsteady diffusion (uD). In addition to the classical approach (FD), the table may also include results obtained using quantum methods (Q).

Table 1: Summary of the selected 1D cases.

1D Cases	Eqn.	Spatial	Temporal	#Eqn.	non/linear	Flow	#Grids	Num.	Focus	Ind.Relev.
Inhomo. Diff.	uD	1D	steady	1	linear	laminar	-	FD+Q	(1,2,3)	40 %
Poisson Eqn.	D	1D	unsteady	1	linear	laminar	-	FD	(1,2)	35 %

3.1.1 Transient Heat Conduction with Non-Uniform Diffusivity

This section presents the results obtained using the classical FD approach for heat transfer problems with inhomogeneous diffusivity on a one-dimensional spatial domain Ω. Unsteady heat conduction is governed by a second-order linear Partial Differential Equation (PDE), which commonly appears in CFD. We employ a non-dimensional formulation, introducing dimensionless spatial and temporal variables $\tilde{x} \in [\tilde{x}_0, \tilde{x}_1]$ and $\tilde{t} \in [0, T_e]$. The corresponding non-dimensional coordinates are defined as $x = \tilde{x}/L$, where $L = \tilde{x}_1 - \tilde{x}_0$, and $t = \tilde{t}/T_e$, where T_e is a characteristic time scale. The material property is spatially varying and is represented by the dimensionless thermal diffusivity $\alpha(x) = \tilde{\alpha}(x)/(VL)$, where $\tilde{\alpha}(x)$ has units of $[m^2/s]$, and V and L are characteristic velocity and length scales, respectively. The governing

This project receives funding from the European Union's Horizon 2020 HORIZON Research and Innovation Actions Programme under Grant Agreement #101080085

second-order PDE describing the temporal evolution of the dimensionless temperature $T = \tilde{T}/T_{\text{ref}}$ is formulated as

$$\begin{aligned} \frac{\partial T}{\partial t} - \frac{\partial}{\partial x}\left(\alpha(x)\frac{\partial T}{\partial x}\right) &= 0 \qquad \text{in } \Omega_{\text{T}} := (0,1)\times(0,\text{T}_{\text{e}}]\,, \\ T(x,t) &= T_{\text{BC}} \qquad \text{on } \partial\Omega\,, \\ T(x,t) &= T_0 \qquad \text{at } t = 0\,. \end{aligned} \tag{1}$$

Equation (1) is solved on the unit space-time domain Ω_{T}. The domain is discretized using $N_{\text{p}} + 2$ equidistantly sampling points $x_k : k \in [0, N_{\text{p}} + 1]$ and $N_{\text{t}} + 1$ equidistant time instants $t^l : l \in [0, N_{\text{t}}]$. The corresponding spatial and temporal step sizes are denoted by Δx and Δt, respectively. A distinction is made between interior grid points, at which Equation (1) is evaluated, and boundary (ghost) points $(x_0, x_{N_{\text{p}}+1})$, which are introduced to enforce the boundary conditions. The discrete form of Equation (1) is obtained by approximating the temporal derivative using a backward finite difference (FD) scheme,

$$\frac{\partial y}{\partial t} = \frac{y^l - y^{l-1}}{\Delta t} + \mathcal{O}(\Delta t)\,. \tag{2}$$

Inhomogeneous material properties, such as a spatially varying thermal diffusivity $\alpha(x)$, frequently occur in engineering applications. To illustrate how such cases can be implemented in a discrete framework, a periodic diffusion operator is considered in the following. The spatial derivatives are approximated through a successive application of backward (outer) and forward (inner) FD schemes, resulting in the following matrix characterizing the dynamics at the interior points

$$\begin{aligned} &\frac{1}{\Delta x^2}\underbrace{\begin{bmatrix} 1 & 0 & \dots & -1 \\ -1 & 1 & \dots & 0 \\ & \ddots & \ddots & \\ 0 & \dots & -1 & 1 \end{bmatrix}}_{\text{backward (outer) FD}}\begin{bmatrix} \alpha_1 & 0 & \dots & 0 \\ 0 & \alpha_2 & \dots & 0 \\ & & \ddots & \\ 0 & \dots & 0 & \alpha_{N_{\text{p}}} \end{bmatrix}\underbrace{\begin{bmatrix} -1 & 1 & \dots & 0 \\ & -1 & 1 & \\ & & \ddots & \ddots \\ 1 & \dots & 0 & -1 \end{bmatrix}}_{\text{forward (inner) FD}}\begin{bmatrix} y_1 \\ y_2 \\ \vdots \\ y_{N_{\text{p}}} \end{bmatrix} \\ &= \frac{1}{\Delta x^2}\begin{bmatrix} -(\alpha_{N_{\text{p}}} + \alpha_1) & \alpha_1 & \dots & \alpha_{N_{\text{p}}} \\ \alpha_1 & -(\alpha_1 + \alpha_2) & \alpha_2 & 0 \\ & \ddots & \ddots & \ddots \\ \alpha_{N_{\text{p}}} & \dots & \alpha_{N_{\text{p}}-1} & -(\alpha_{N_{\text{p}}-1} + \alpha_{N_{\text{p}}}) \end{bmatrix}\begin{bmatrix} y_1 \\ y_2 \\ \vdots \\ y_{N_{\text{p}}} \end{bmatrix} \approx \frac{\partial}{\partial x}\left(\alpha(x)\frac{\partial}{\partial x}y(x,t)\right)\,. \end{aligned} \tag{3}$$

This first benchmark considers Dirichlet boundary conditions imposed at both ends of the domain, with $T|_{x=0} = 0$ and $T|_{x=1} = 1$, and an initial temperature distribution given by $T(x, t = 0) = 0$. The simulations are performed using a total of $N_{\text{p}} = 16$ and $N_{\text{p}} = 64$ interior points, plus the two ghost points at the boundaries. The thermal diffusivity $\alpha(x)$ follows a Gaussian profile with a maximum at the center of the domain, namely $\alpha(x) = 1 + \exp\left(-100\,(0.5 - x)^2\right)$. The spatially varying heat flux is represented through the contributions $-\alpha_{k-1} - \alpha_k$ and α_k, as given in Equation (3).

Figure 1 illustrates the results obtained using the classical FD approach with a constant time step of $\Delta t = 0.018$, independent of the discretization. The spatio-temporal evolution of the predicted temperature $T(x, t)$ for $N_{\text{t}} + 1 = 40$ time steps and $N_{\text{p}} = 64$ is shown in Figure 1a, where the abscissa represents the spatial coordinate and the ordinate represents the normalized time. Figure 1b also shows spatial temperature profiles obtained for $N_{\text{p}} = 16$, at six representative time instants. The slope of the steady-state profiles is reduced by half in the center of the domain due to the doubling of the diffusivity α.

The complete data of this benchmark case can be found at the following link doi.org/10.25592/uhhfdm.16634 and it is part of a publication in the engineering journal *AIAA*, cf. Ref. [2].

3.1.2 Non-constant material and grid in Poisson equation

In this section, we consider the one-dimensional Poisson equation governing a steady diffusion problem defined on the unit interval $x \in (0, 1)$, viz.

$$-\frac{d}{dx}\left(\nu(x)\frac{d\phi}{dx}\right) = f(x)\,, \tag{4}$$

This project receives funding from the European Union's Horizon 2020 HORIZON Research and Innovation Actions Programme under Grant Agreement #101080085

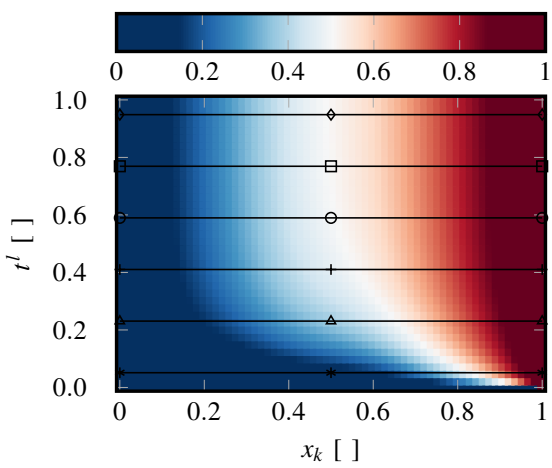

(a) FD predicted temperature evolution for $N_\mathrm{p} = 64$ with lines and symbols marking the equidistant time instants used to extract spatial temperature profiles in Subfig. (b).

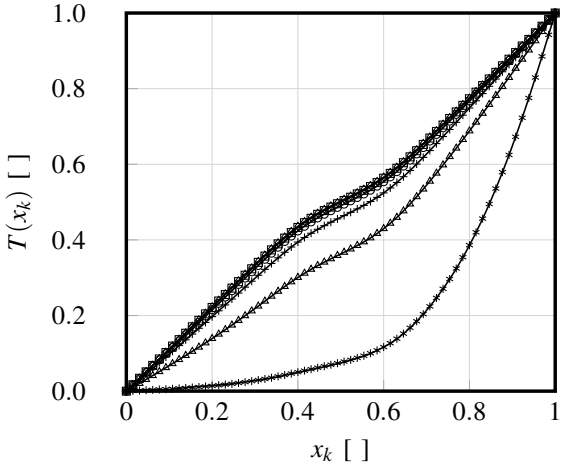

(b) Spatial temperature profiles computed by the FD method for $N_\mathrm{p} = 64$ at the six time instants given in Subfig. (a).

Figure 1: Transient heat conduction results on $N_\mathrm{p} = 64$ interior points.

where $\nu(x) > 0$ is the spatially varying material property (diffusion coefficient), $\phi(x)$ is the unknown function, and $f(x)$ is a given source term. The boundary conditions are given by $\phi(0) = \phi_0$, $\phi(1) = \phi_1$, with prescribed constants ϕ_0 and ϕ_1. The domain is discretised using an inhomogeneous mesh consisting of $N_\mathrm{p} + 2$ nodes with coordinates $0 < x_0 < x_1 < \cdots < x_{N_\mathrm{p}} < 1$. We distinguish between interior points N_p and ghost (boundary) points, which serve to introduce boundary conditions. Generally, variables located at the boundaries can either be part of the unknowns or moved to the right-hand side. In the latter case, employed here, the boundary conditions are represented by the influence of prescribed ghost point variables on the interior point approximations. In the case of Neumann or Robin conditions, this usually involves the additional discretization of the spatial derivative. This technique allows us to align with VQA-development of WP3 as well as existing literature [2, 3, 4, 5]. We approximate the differential operator by applying the finite difference method on the non-uniform grid. To this end, we employ first-order accurate central differences and discretize the Equation (4) following the product rule. The discretised equation at the interior node i is given by

$$-\frac{1}{\Delta x_i}\left(\nu_{i+1/2}\frac{\phi_{i+1}-\phi_i}{\Delta x_i}\right)+\frac{1}{\Delta x_{i-1}}\left(\nu_{i-1/2}\frac{\phi_i-\phi_{i-1}}{\Delta x_{i-1}}\right)=f_i\,, \tag{5}$$

where the half-node diffusivities are defined as $\nu_{i+1/2} = \nu\left(\frac{x_i+x_{i+1}}{2}\right)$.

Rearranging the discrete problem into a matrix/vector format, leads to a linear system of equations written as $A\phi = f$, where the unknown vector is $\phi = (\phi_1, \phi_2, \ldots, \phi_{N_\mathrm{p}})^T$, and the matrix $A \in \mathbb{R}^{N_\mathrm{p}\times N_\mathrm{p}}$ is a sparse tridiagonal matrix representing the discretised operator incorporating the variable coefficients and non-uniform spacing. For benchmarking purposes, consider $\nu(x) = 1 + \exp\left(-100\,(0.5-x)^2\right)$, with homogeneous boundary conditions $\phi_0 = 0$, $\phi_1 = 0$. The domain is discretised with $N_\mathrm{p} = 2^n$ nodes, where $n = 2, 4, 6$ and 8, using an inhomogeneous discretization described by

$$\Delta x_i = 1.2\Delta x_{i-1}\,. \tag{6}$$

The results for the four discretizations are obtained by solving with the matrix inverse, viz. $A^{-1}f = \phi$, and are illustrated in Figure 2. The displayed results are obtained for a coarse grid, featuring $N_\mathrm{p} = 4$ interior points, a medium grid with $N_\mathrm{p} = 16$ interior points, a fine $N_\mathrm{p} = 64$ discretization, and an extra fine grid, featuring $N_\mathrm{p} = 256$ interior points. For an application on quantum computers, the inhomogeneous structure of the matrix A is particularly challenging and a focal point of this benchmark. The benchmark-related data is accessible via the DOI:doi.org/10.25592/uhhfdm.18563.

This project receives funding from the European Union's Horizon 2020 HORIZON Research and Innovation Actions Programme under Grant Agreement #101080085

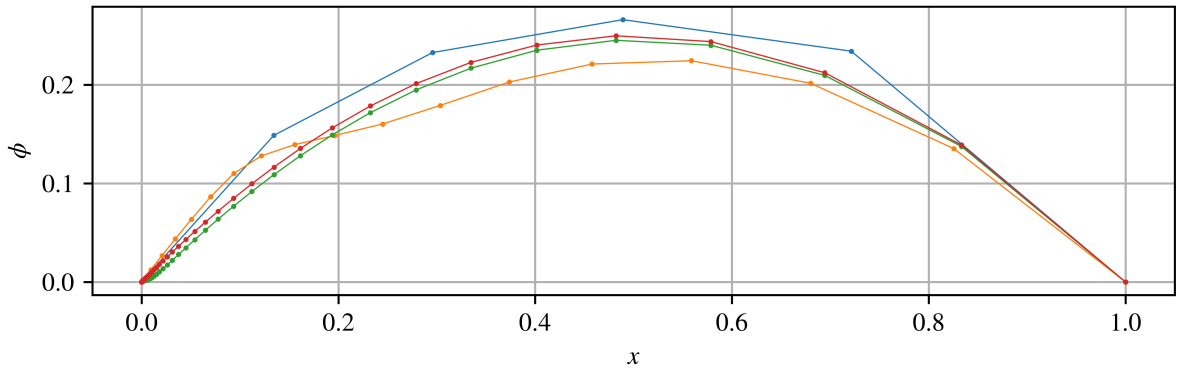

Figure 2: FD predicted spatial distribution of ϕ for $N_p = 4$ (blue) , 16 (orange) , 64 (green) and 128 (red) points. Symbols mark the discrete locations.

3.2 2D Problems

This second section presents the results obtained from selected two-dimensional (2D) benchmark cases relevant to thermo-fluid dynamic computational simulations. The chosen examples serve as a standardized test set for validating quantum algorithms for 2D flow and heat transfer problems. In addition to classical FD approaches, results obtained from Finite Volume (FV) methods are included.

As the first application pointing towards final battery cooling, the consortium has addressed the double-bent channel flow simulation. To this end, the initial case in D1.1 [1] was taken up again, in which the geometry was discretized by a Cartesian grid and modeled by an immersed boundary approach, and simulated with an FV discretization. To ensure numerical robustness and reliability, a comprehensive grid sensitivity study accompanies this test case. Furthermore, body-fitted, curvilinear grids are addressed in Sec. 3.2.3.

Table 2 summarizes the key attributes of all 2D benchmark problems, highlighting their physical modeling focus and engineering relevance. The benchmarks address several critical phenomena, including: (1) boundary conditions, (2) non-homogeneous meshes, (3) non-homogeneous advection effects, (4) transient and unsteady flow behavior, (5) interplay between advection and diffusion, (6) nonlinear flow dynamics, and (7) multiphysics modeling of conjugate heat transfer between fluid and solid. The governing equations encompass a range of problem types, denoted as diffusion (D), unsteady diffusion (uD), unsteady advection-diffusion (uAD), unsteady convection-diffusion (uCD), and conjugate heat transfer (CH). In addition to standard numerical techniques such as Finite Difference (FD) and Finite Volume (FV) methods, the table also includes references to comparative results obtained using quantum computer-based methods (Q).

Table 2: Summary of selected 2D cases.

2D Cases	Eqn.	Spatial	Temporal	#Eqn.	non/linear	Flow	#Grids	Num.	Focus	Ind.Relev.
TGV Adv. Diff.	uAD	2D	unsteady	1	linear	laminar	-	FD+Q	3,5	55%
Heat Conduc.	uD	2D	unsteady	1	linear	laminar	-	FD+Q	1,4	60%
Curvilinear cases	uCD	2D	unsteady	2	nonlinear	laminar	3	FD+Q	1,2,6	65%
S-Bent Ducts	CD	2D	steady	2	nonlinear	laminar	3	FV	1,6,7	90%
Buoyancy Flows	uCD/CH	2D	unsteady	3	nonlinear	turbulent ($Ra \geq 10^8$)	2	FV	1,4,6,7	85%

3.2.1 Taylor-Green Vortex-like advection-diffusion problem

A prominent PDE in fluid dynamics is the advection-diffusion equation, which has also been covered in Ref. [6]. This passive scalar transport equation reads

$$\frac{\partial \phi}{\partial t} + \vec{v} \cdot \nabla \phi = D \nabla^2 \phi \,, \tag{7}$$

which describes the advection of a scalar quantity $\phi(\mathbf{x}, t)$ by an incompressible velocity field $\vec{v}(\mathbf{x})$ in a medium with diffusivity D. The incompressibility condition enforces $\nabla \cdot \vec{v} = 0$. The spatial do-

This project receives funding from the European Union's Horizon 2020 HORIZON Research and Innovation Actions Programme under Grant Agreement #101080085

main is assumed to be two-dimensional, periodic over $x, y \in [0, 2\pi)$, with the coordinates $\mathbf{x} = [x, y]^T$ and discretized equidistantly using $\sqrt{N_\mathrm{p}}$ supporting points per dimension. For spatial discretization of Equation (7), first-order central and second-order central FD schemes are employed to transform the PDE into a system of ordinary differential equations (ODEs)

$$\frac{d\vec{\phi}}{dt} = M\vec{\phi}\,, \tag{8}$$

where $\vec{\phi}(t)$ is the discrete scalar field vector and M is a matrix encoding the discretized advection and diffusion operators. Time integration can be performed using an explicit time-marching scheme such as the forward Euler method, which updates the scalar field by $\vec{\phi}(t + \Delta t) = A\vec{\phi}(t), \quad \text{with} \quad A = I + M\Delta t\,,$ where I is the identity matrix and Δt is the time step size. For spatial and temporal constant velocity, the explicit matrix A takes a banded form

$$A = \begin{bmatrix} 1-2r_d & r_d - \frac{r_a}{2} & & 0 & r_d + \frac{r_a}{2} \\ r_d + \frac{r_a}{2} & \ddots & \ddots & & 0 \\ & \ddots & \ddots & \ddots & \\ 0 & & \ddots & \ddots & r_d - \frac{r_a}{2} \\ r_d - \frac{r_a}{2} & 0 & & r_d + \frac{r_a}{2} & 1-2r_d \end{bmatrix}, \tag{9}$$

where $r_a = v\Delta t/\Delta x$ and $r_d = D\Delta t/(\Delta x)^2$ are the advective and diffusive stability parameters, respectively.

For illustrative purposes, the domain is discretized on a 64×64 uniform grid, yielding $N_\mathrm{p} = 4096$ points. In quantum simulation terms, this would correspond to a 12-qubit quantum register. The scalar field $\phi(x, y, 0)$ is initialized proportionally to $\sin(x + y) + 1$ and normalized to have unit norm, i.e., $\vec{\phi}(0) \propto \sin(x + y) + 1$ with $\|\vec{\phi}(0)\| = 1$. Furthermore, the velocity field is initialized over the periodic domain $[0, 2\pi) \times [0, 2\pi)$ like a two-dimensional Taylor-Green vortex problem as it is illustrated in Figure 3, defined by the steady velocity

$$\vec{v}(x, y) = \begin{bmatrix} \sin(x)\cos(y) \\ -\cos(x)\sin(y) \end{bmatrix}. \tag{10}$$

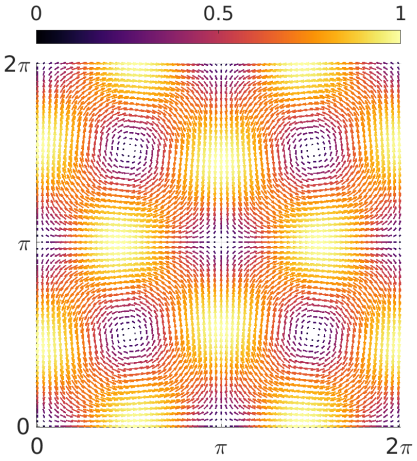

Figure 3: Steady TGV-like velocity field $\vec{v}(x, y)$.

The simulation employs an explicit forward Euler time stepping and runs for a total number of $N_\mathrm{t} = 1400$ time steps. The stability parameters are set to ensure numerical convergence, such that the maximal advective Courant number is $\max(r_a) = 0.1$ and the diffusive stability parameter $r_d = 0.1$. The Péclet number, representing the ratio of advective to diffusive transport, is estimated as

$$Pe = \frac{v_\mathrm{rms}\pi}{D} = 23\,, \tag{11}$$

This project receives funding from the European Union's Horizon 2020 HORIZON Research and Innovation Actions Programme under Grant Agreement #101080085

where the root-mean-square velocity is $v_{\text{rms}} = 1/\sqrt{2}$. This indicates that the advection dominates the transport process, while diffusion plays a role at larger time scales.

The results from the classical numerical simulation, applying the matrix A directly, reveal that the scalar field evolves toward a spatially uniform steady state equal to the spatial mean of the initial condition mean($\vec{\phi}(0)$). The contour evolution plots in Figure 4 illustrate the gradual advection-driven stirring of the scalar field by the Taylor-Green vortex, with diffusion smoothing gradients over time. The stability and fidelity of the forward Euler time marching scheme demonstrate the suitability of this approach for simulating advection-diffusion phenomena in 2D fluid flows, and provide a platform to benchmark emerging quantum algorithms for PDE simulation.

The data is accessible via the DOI: doi.org/10.25592/uhhfdm.18565 and has been utilized in Ref. [6], published in *Physical Review A*, for benchmarking.

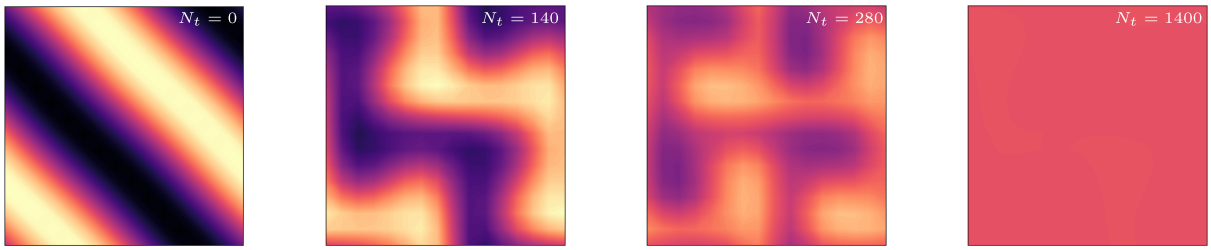

Figure 4: Solutions for the tracer scalar ϕ transported by a TGV-like velocity field $\vec{v}(\mathbf{x})$, illustrated for $N_t = 0$, 140, 280, and 1400 time steps.

3.2.2 Unsteady Heat Equation including Boundary conditions

Consider a two-dimensional spatial domain with coordinates $\vec{x} \in [0,1] \times [0,1]$ [m], time $t \in [0,T)$ [s], a scalar temperature field T [K], and a constant dynamic viscosity D [m^2/s]. The dynamics of the system are governed by the unsteady diffusion equation, for instance, describing heat conduction, viz.

$$\frac{\partial \phi}{\partial t} - D\,\nabla^2 \phi = 0\,. \tag{12}$$

This parabolic PDE is discretized using uniform and isotropic spatial and temporal grid spacings Δx [m] and temporal Δt [s], with $N = N_{\text{x}_1}^d$ spatial points and N_{t} time steps, respectively. For clarity, the discretization of Equation (12) is presented for the one-dimensional case, using $N_{\text{x}_1} = \sqrt[d]{N}$ grid points. The differential operators are approximated using a first-order explicit forward Euler scheme in time and second-order central FDs in space. In addition, periodic boundary conditions are assumed for simplicity. Under these assumptions, the discrete form of Equation (12) can be written as

$$\frac{\phi_j^{t+1} - \phi_j^t}{\Delta t} - D\frac{\phi_{j+1}^t - 2\phi_j^t + \phi_{j-1}^t}{\Delta x^2} = 0\,. \tag{13}$$

Rewriting the discretized system into a matrix/vector format results in a matrix $A \in \mathbb{R}^{N\times N}$, viz.

$$A = \begin{bmatrix} 1-2r_{\text{h}} & r_{\text{h}} & & 0 & r_{\text{h}} \\ r_{\text{h}} & 1-2r_{\text{h}} & \ddots & & 0 \\ & \ddots & \ddots & \ddots & \\ 0 & & \ddots & 1-2r_{\text{h}} & r_{\text{h}} \\ r_{\text{h}} & 0 & & r_{\text{h}} & 1-2r_{\text{h}} \end{bmatrix}, \tag{14}$$

which acts as the time-marching operator in $\boldsymbol{\phi}(t+\Delta t) = A\boldsymbol{\phi}(t)$. The dimensionless parameter $r_{\text{h}} = D\,\Delta t/\Delta x^2$ [-] defines the spatio-temporal diffusion behavior.

Using this time-marching formulation, Equation (13) is advanced sequentially in time. The choice of time step is constrained by stability requirements determined by r_{h}. This imposes a convergence condition

This project receives funding from the European Union's Horizon 2020 HORIZON Research and Innovation Actions Programme under Grant Agreement #101080085

on the numerical scheme applied to the resulting system of ODEs, requiring that all solution remain bounded by values below one throughout the entire simulation.

The method of images imposes boundary conditions by extending the field through reflections at the domain boundaries, making use of the symmetric and antisymmetric characteristics of Neumann and Dirichlet conditions, respectively. This procedure results in a doubling of the degrees of freedom for each non-periodic dimension, which reduces its efficiency in classical computational settings. On a quantum computer, however, such symmetry-based reflections can be realized more efficiently by allocating a single qubit per non-periodic dimension, thereby leveraging exponential scaling. This approach allows boundary conditions to be incorporated via either even (sign-preserving) or odd (sign-changing) symmetry between neighboring points, while still utilizing discrete periodic operators.

Table 3: Boundary modifications on the matrix A in Equation (14)

	$a_{1,1}$	$a_{1,N}$	$a_{N,1}$	$a_{N,N}$
Periodic	$1-2r_\mathrm{h}$	r_h	r_h	$1-2r_\mathrm{h}$
Dirichlet	$1-2r_\mathrm{h}$	0	0	$1-2r_\mathrm{h}$
Neumann	$1-r_\mathrm{h}$	0	0	$1-r_\mathrm{h}$

The implementation of boundary conditions using the method of images is examined for homogeneous Neumann, Dirichlet, and mixed boundary types. For all cases, the initial condition at $t = 0$ is defined by a two-dimensional Gaussian perturbation of the form $\phi(\vec{x}) = \exp\big(-200(x_1 - 0.25)^2 - 200(x_2 - 0.25)^2\big)$, located in the lower-left region of the domain.

The FD results for T^t with homogeneous Neumann conditions computed for $N_\mathrm{t} = 12000$ explicit time steps with $r_\mathrm{h} = 0.2$ are depicted in Figure 5. The even (symmetric) reflection on the three additional quadrants II, III, and IV, is not shown in Figure 5, only the domain of interest is given. The full resolution contains 128×128 grid points, where $N = 64 \times 64$ points correspond to the (non-reflected) domain of interest in quadrant I.

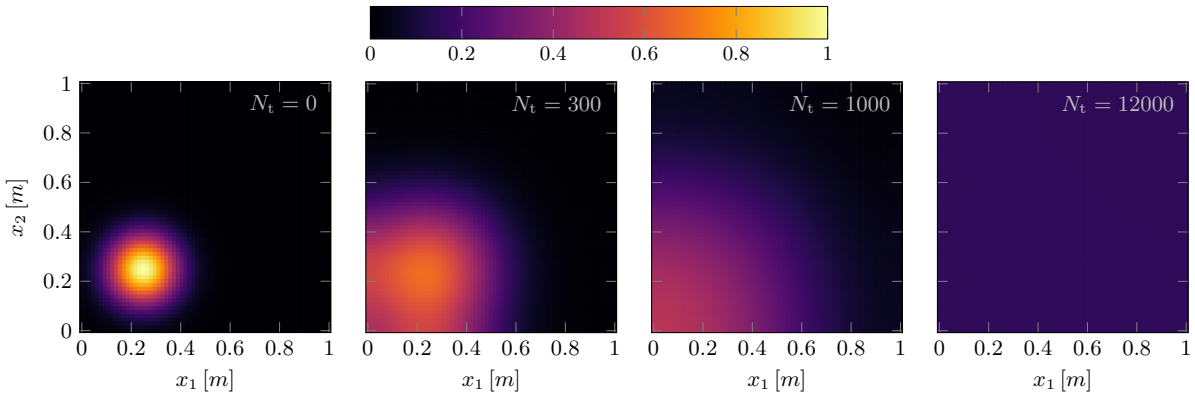

Figure 5: FD results for the temperature field T^t governed by the two-dimensional heat equation (Equation (12)) with homogeneous Neumann boundary conditions enforced by the method of images. Results refer to 128×128 grid points (including reflection quadrants) obtained from simulation for $N_\mathrm{t} = 12000$ time steps with $r_\mathrm{h} = 0.2$.

Homogeneous Dirichlet boundary conditions are implemented by adapting the type of reflection used. In particular, the method of images applies an odd (antisymmetric) reflection to the initial conditions. The full computational domain is resolved with 128×128 grid points, of which $N = 64\times64$ are dedicated to the quadrant of interest (quadrant I). The numerical solution of Equation (13) is advanced over $N_\mathrm{t} = 12000$ time steps in combination with $r_\mathrm{h} = 0.2$. The resulting evolution of T^t is depicted in Figure 6 at four representative time instants ($N_\mathrm{t} = 0$, 300, 1000 and 12000) of the FD temporal simulation in quadrant I.
To conclude, homogeneous mixed boundary conditions are simulated with the previously described method. In the configuration studied, Neumann conditions are imposed on the boundaries with out-

This project receives funding from the European Union's Horizon 2020 HORIZON Research and Innovation Actions Programme under Grant Agreement #101080085

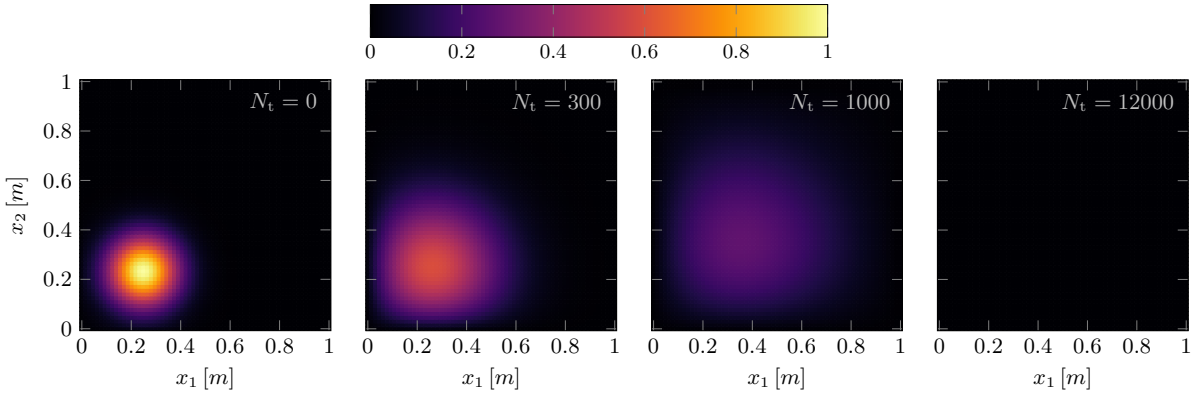

Figure 6: Benchmarking of FD results for the two-dimensional heat equation (Equation (12)) with homogeneous Dirichlet boundary conditions enforced by the method of images. Results refer to 128×128 grid points (including reflection quadrants). Simulation for $N_t = 12000$ time steps with $r_h = 0.2$.

ward normals in the x_1-direction, while Dirichlet conditions are applied along the x_2-direction. This corresponds to an even (symmetric) reflection in the x_1-direction and an odd (antisymmetric) reflection in the x_2-direction of the initial condition. The FD simulation is executed over $N_t = 12000$ time steps with the stability parameter of $r_h = 0.2$. The total spatial discretization consists of 128×128 grid points, including the reflected regions in quadrants II, III, IV, where $N = 64 \times 64$ points represent the physical domain of interest in quadrant I. Figure 7 illustrates the temporal evolution of T^t in quadrant I at four representative time instants, i.e., $N_t = 0$, 300, 1000 and 12000. The influence of the different boundary conditions on the spatial distribution of T^t is clearly visible.

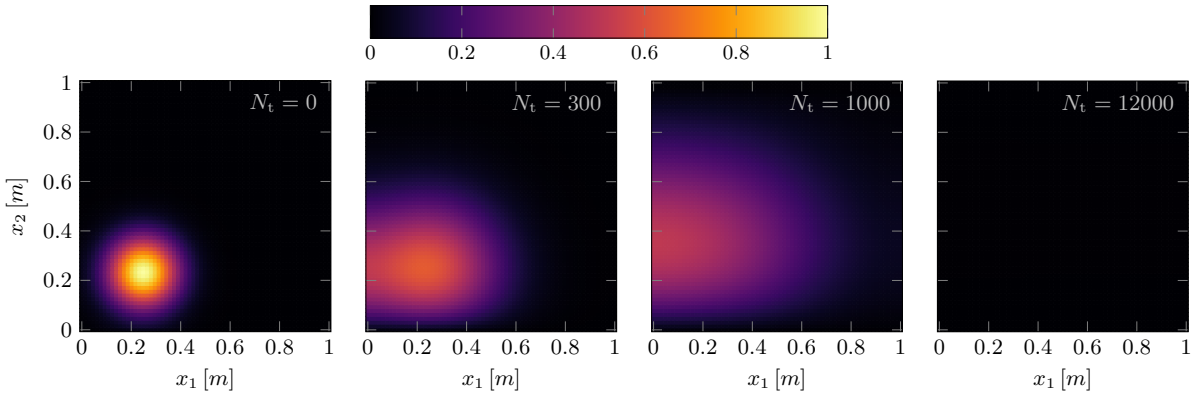

Figure 7: FD results for the two-dimensional heat equation (Equation (12)) with homogeneous mixed boundary conditions implemented by the method of images are presented. Homogeneous Neumann conditions are applied along the horizontal direction, while homogeneous Dirichlet conditions are imposed in the vertical direction. The results are based on a spatial resolution of 128×128 grid points, including the reflected quadrants. The simulation is performed over $N_t = 12000$ time steps with a stability parameter of $r_h = 0.2$.

This dataset is available via the DOI-link: doi.org/10.25592/uhhfdm.18048 and it is also used as a benchmark in the publication Ref. [7] published at the *International Journal for Numerical Methods in Engineering*.

3.2.3 Flow around a cylinder using body-fitted grids

The two-dimensional laminar flow of a Newtonian fluid with constant density $\tilde{\rho}$ in the physical domain Ω is described by the incompressible Navier–Stokes equations. To this end, the following case covers the flow around a cylinder, employing curvilinear coordinates for discretization. Introducing the following dimensionless variables: $\vec{x} = \tilde{\vec{x}}/L$, $\vec{v} = \tilde{\vec{v}}/U_\infty$, $t = \tilde{t}/T_{\text{ref}}$, and $p = \tilde{p}/P_{\text{ref}}$, the governing equations

This project receives funding from the European Union's Horizon 2020 HORIZON Research and Innovation Actions Programme under Grant Agreement #101080085

become

$$\begin{aligned} \frac{\partial \vec{v}}{\partial t} + (\vec{v} \cdot \vec{\nabla})\vec{v} &= -\vec{\nabla} p + \frac{1}{Re}\Delta \vec{v} + \vec{f} \quad \text{in } \Omega, \\ \vec{\nabla} \cdot \vec{v} &= 0 \qquad\qquad\qquad\quad \text{in } \Omega\,, \end{aligned} \tag{15}$$

where $\vec{\nabla}$ denotes the gradient operator with respect to the non-dimensional spatial coordinates, and $Re = U_\infty L/\tilde{\nu}$ is the Reynolds number. The convective reference time is given by $T_{\text{ref}} = L/U_\infty$, with U_∞ representing the reference (free-stream) velocity, $\tilde{\nu}$ the kinematic viscosity of the fluid, and L a characteristic length, typically chosen as the diameter D of the cylinder studied. Figure 8 illustrates the computational setup for the two-dimensional flow around a cylinder of unit diameter D. The cylinder boundary Γ is centered within a circular physical domain Ω, whose outer boundary $\partial\Omega$ is a circle with diameter $32D$. The reference pressure is defined as $P_{\text{ref}} = \tilde{\rho} U_\infty^2$, and the non-dimensional volume-

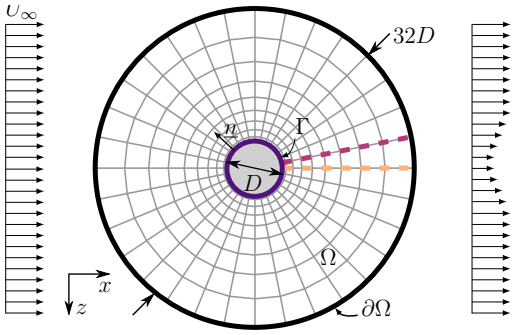

Figure 8: Dimensionless representation of the discretized 2D cylinder flow domain. The block-structured O-type grid is illustrated with light-gray lines, while the domain boundaries are highlighted in black (outer boundary) and magenta (cylinder surface), cf. [8].

specific body force is expressed as $\vec{f} = \tilde{\vec{f}} L/U_\infty^2$. The initial condition for the velocity field is prescribed as $\vec{v}(\vec{x}, 0) = \vec{v}_{\text{init}}(\vec{x})$. The boundary conditions are specified as follows. On the surface of the object, denoted by Γ, no-slip Dirichlet conditions are applied to the velocity, $\vec{v} = \vec{v}_\Gamma$, while a natural Neumann condition is imposed for the pressure:

$$\begin{aligned} \vec{v} - \vec{v}_\Gamma = \vec{0}, \quad \vec{\nabla} p \cdot \vec{n} = 0, \quad \text{on } \Gamma, \\ \vec{v} - \vec{v}_\infty = \vec{0}, \qquad p = 0, \quad \text{on } \partial\Omega, \end{aligned} \tag{16}$$

where $\vec{n}$ is the outward unit normal vector to the boundary. On the exterior boundary $\partial\Omega$, Dirichlet conditions are enforced for both velocity and pressure. The boundary conditions are implemented via a ghost-point method, which introduces additive correction terms to the discrete differential operators, while the boundary points themselves are excluded from the solution vector [9]. Thereby, the benchmark aligns to common quantum practice as discussed in Ref. [3]. Contributions to the source term $\vec{f}$ due to volume-specific body forces are neglected in this study.

The problem is discretized with FDs. To this end, the spatial discretization of the two-dimensional physical domain Ω employs a structured O-type grid, denoted by $\mathcal{G}$ and the physical coordinates (x_{ij}, z_{ij}) are obtained through a mapping from a unit-square computational domain Ω_0, implemented via a transfinite interpolation method [10]. Within the computational domain, the interior grid points are specified by the coordinates $\eta_{ij} = (i+1)\,\delta\eta$, $\xi_{ij} = j\,\delta\xi$. Defining N_η and N_ξ establishes an $N_\eta \times N_\xi$ uniform grid with mesh spacings $\delta\eta = \frac{1}{N_\eta+1}$, $\delta\xi = \frac{1}{N_\xi}$. The indices $i = -1$ and $i = N_\eta$ correspond to the inner (top) and outer (bottom) boundaries of the domain Ω (and equivalently Ω_0). The computational grid is treated as periodic along the ξ-direction. Next, a coordinate transformation $\Phi : \Omega_0 \to \Omega$ is introduced, which maps the computational coordinates (ξ_{ij}, η_{ij}) to the physical coordinates (x_{ij}, z_{ij}), with $x_{ij} = x(\xi_{ij}, \eta_{ij})$, $z_{ij} = z(\xi_{ij}, \eta_{ij})$, as depicted by the light-gray lines in Figure 8. To assess the impact of mesh refinement, three nested grids with uniform spacing in the circumferential direction are considered: $\mathcal{G}_1 : \quad N = 256 \times 256\,, \quad \mathcal{G}_2 : \quad N = 256 \times 512\,, \quad \mathcal{G}_3 : \quad N = 512 \times 512\,,$ where N denotes the total number of grid points. The minimum grid spacing near the cylinder surface, defined as the smaller of the

This project receives funding from the European Union's Horizon 2020 HORIZON Research and Innovation Actions Programme under Grant Agreement #101080085

radial grid spacing and the local circumferential arc length, is approximately $h_{\min} \approx 6.78 \times 10^{-3}$, for $\mathcal{G}_1$, 6.14×10^{-3}, for $\mathcal{G}_2$, and 3.39×10^{-3}, for $\mathcal{G}_3$. Again, all lengths are normalized by the cylinder diameter D, so that $h_{\min} = \tilde{h}_{\min}/D$ denotes the smallest non-dimensional step size in physical space, typically observed at the inner radial boundary adjacent to the cylinder surface. Analytic descriptions of the discretizations are available in Ref. [8]. The use of this curvilinear discretization permits approximating the spatial derivatives present in the momentum and continuity Equations (15) within the computational domain Ω_0. To this end, the differential operators are approximated by equidistant second-order central difference schemes.

The computational framework is completed by the use of Chorin's [11] fractional step method, enabling time evolution from $t^{(m)}$ to $t^{(m+1)} = t^{(m)} + \delta t$. In this process, an intermediate velocity field $\vec{v}^*$ is computed by solving the momentum equations without the pressure gradient. Subsequently, the intermediate velocity field $\vec{v}^*$ is corrected to enforce incompressibility by solving the pressure Poisson equation. The velocity at the new time level $t^{(m+1)}$ is then updated by subtracting the pressure gradient contribution. In this regard, the given numerical setup is applied to analyze the flow past a stationary cylinder under steady ($Re = 20$) and unsteady ($Re \geq 50$) flow regimes (cf. Sec. 3.2.4), and for transient flow behavior around a rotating cylinder at Reynolds number $Re = 100$ (cf. Section 3.2.5).

3.2.4 Non-Rotating Cylinder

Steady Flow ($Re = 20$) The steady-state solutions of the dimensionless Navier-Stokes equations are computed at Reynolds number $Re = 20$ covering the discretizations $\mathcal{G}_1$, $\mathcal{G}_2$, and $\mathcal{G}_3$ by numerically integrating a pseudo-transient initial value problem. Therefore, the time variable t is treated as a pseudotime, which parametrizes the evolution from initial conditions to the steady state. To ensure numerical stability for the convective term, the maximum flow velocity is estimated by scaling the free-stream velocity, $U_{\max} = \gamma U_\infty$, with a conservative factor $\gamma = 1.5$, following established guidelines in the literature (see Ref. [9]). Consequently, the pseudotime step size δt_k for each grid $\mathcal{G}_k$ is chosen such that the associated convective Courant number remains below unity $\delta t_k = \tilde{\delta t}_k D/U_\infty$, with values $\delta t_1 = 4.5 \times 10^{-3}$, $\delta t_2 = 3.8 \times 10^{-3}$, $\delta t_3 = 1.1 \times 10^{-3}$, respectively. The evolution is done till convergence, requiring 30 flow-through times. Figure 9 shows the converged flow field for the finest discretization at 8100 pseudo time steps. Moreover, Figure 9 includes an inset that magnifies the isoline for direct comparison and emphasizes the classical Föppl vortex pair behind the cylinder. To assess the characteristics of the numerical method, the coefficient of drag $C_{\mathrm{D}} = 2\tilde{F}_{\mathrm{D}}/(\tilde{\rho} U_\infty^2 D)$, has been computed for all three discretizations and is listed in Tab. 4. The value increases with refined discretization. Moreover, the results confirm that the coefficient of drag is more sensitive to a grid refinement in the circumferential direction, which explains the increase from $\mathcal{G}_2$ to $\mathcal{G}_3$. For proof of concept, it is confirmed that the values are in the range and consistency is confirmed.

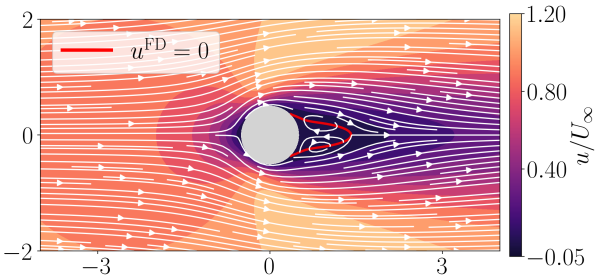

Figure 9: Streamline visualization for the flow around a cylinder at Reynolds number $Re = 20$ and indication of contours of the normalized horizontal velocity component (u) associated with the colorbar. Furthermore, the zero-horizontal-velocity ($u = 0$) isoline is emphasized by a solid red line.

Unsteady Flow ($Re = 150$) The analysis of the unsteady flow regimes that develop for Reynolds numbers $Re \geq 50$ marks another avenue within this experiment. Therefore, transient simulations are conducted on the two coarser grids, $\mathcal{G}_1$ and $\mathcal{G}_2$, employing time steps of $\delta t_1 = \tilde{\delta t}_1 U_\infty/D \approx 3.4 \times 10^{-3}$, and $\delta t_2 = \tilde{\delta t}_2 U_\infty/D \approx 3.1 \times 10^{-3}$, respectively. The maximum velocity is estimated as $U_{\max} = \gamma U_\infty$, with $\gamma = 2$, ensuring that the Courant number remains below unity for all Reynolds numbers

This project receives funding from the European Union's Horizon 2020 HORIZON Research and Innovation Actions Programme under Grant Agreement #101080085

Table 4: Coefficient of Drag C_{D} sensitivity study along discretization $\mathcal{G}_1$, $\mathcal{G}_2$ and $\mathcal{G}_3$ at Reynolds number $Re = 20$.

Discretization	$\mathcal{G}_1$	$\mathcal{G}_2$	$\mathcal{G}_3$
Coeff. of Drag C_{D}	2.047	2.057	2.097

considered. Given an expected Strouhal number of $St \approx 0.2$, this corresponds to approximately 60 time steps per vortex shedding period. For algorithmic enhancement, transient behavior is triggered by introducing asymmetry into the initial velocity field via a perturbation in the form of a 5% velocity modulation. The modulation is accomplished by setting the initial flow field to

$$u_{ij}(t=0) = A_0 \frac{e^{(i\delta\eta)^6} - 1}{e - 1} \sin\left(2\pi j \delta\xi\right), \tag{17}$$

where the perturbation amplitude is set to $A_0 = 0.05$. This formulation introduces an asymmetry relative to the branch cut for triggering vortex shedding while ensuring that the modulation intensity diminishes radially toward the far-field boundary $\partial\Omega$. Figure 10 shows a representative snapshot of the velocity magnitude $|v|$ at $Re = 150$ for the finite-difference simulation. This snapshot corresponds to approximately 85 passage times (roughly 2.5×10^4 time steps) on the coarse grid $\mathcal{G}_1$, for which the flow has reached a periodic state. Again, to assess the grid convergence, the Strouhal number has been computed and is listed in Tab. 5.

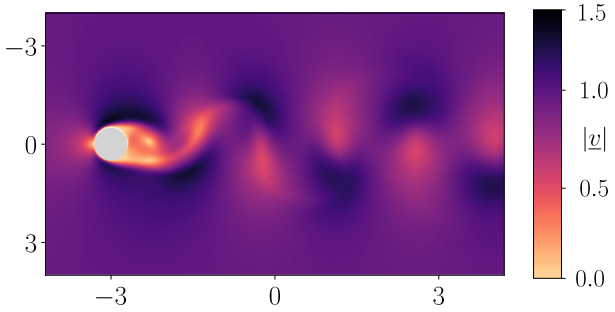

Figure 10: Velocity magnitude $|v|$ snapshot at $Re = 150$ using grid $\mathcal{G}_1$, at approximately 85 flow passes.

Table 5: Strouhal number St sensitivity study for discretizations $\mathcal{G}_1$ and $\mathcal{G}_2$.

Discretization	$\mathcal{G}_1$	$\mathcal{G}_2$
Strouhal number	0.18447	0.18497

3.2.5 Rotating Cylinder

Instead of a stationary cylinder, we investigate a scenario known to exhibit the classical Magnus effect at a Reynolds number of $Re = 100$. Therefore, the cylinder surface is subject to a no-slip boundary condition with a prescribed non-zero tangential velocity $U_\Gamma = \dot{\theta} U_\infty$, where the dimensionless angular velocity $\dot{\theta} = \frac{D\dot{\delta}}{2U_\infty} = 1.0$ is set. At the discrete boundary points, the components of the normalized velocity vector $\vec{v}_\Gamma$ are prescribed as

$$\begin{aligned} u_{\Gamma_j} &= \dot{\theta}\, \sin(2\pi j\, \delta\xi), \\ v_{\Gamma_j} &= -\dot{\theta}\, \cos(2\pi j\, \delta\xi), \end{aligned} \qquad j = 0, \ldots, N_\xi - 1, \tag{18}$$

where N_ξ denotes the number of discretization points along the cylinder circumference. For a proof of concept, this experiment only covers discretization $\mathcal{G}_1$.

The initial condition is chosen as a uniform flow, $\vec{v}_{\mathrm{init}} = (U_\infty, 0)^\top$. The sign convention corresponds to a counter-clockwise rotation of the cylinder. This rotation induces a net time-averaged circulation

This project receives funding from the European Union's Horizon 2020 HORIZON Research and Innovation Actions Programme under Grant Agreement #101080085

around the body, which primarily manifests as a phase shift in the lift force oscillations. The time-averaged coefficient of lift results in $C_{\mathrm{L}} = 2.49$ at a Strouhal number of $St = 0.1663$. Figure 11 shows the corresponding velocity magnitude fields predicted at timesteps $\tilde{t}U_\infty/D = 4$ and $\tilde{t}U_\infty/D = 15$.

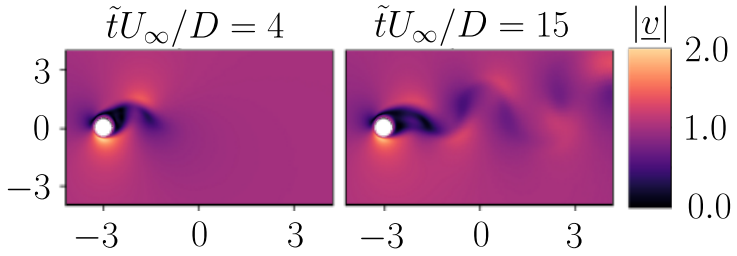

Figure 11: Velocity magnitude fields at non-dimensional times $\tilde{t}U_\infty/D = 4$ (left) and $\tilde{t}U_\infty/D = 15$ (right).

The benchmark dataset is available via the DOI: doi.org/10.25592/uhhfdm.17687 and is also used as a benchmark along with the Ref. [8], which is published at *Computer Physics Communications*.

3.2.6 Immersed-boundary based Geometry representation of the S-Bent in a Box

The double-bent channel represents a simplified example of the BEV cooling case, shown in Section 3.3.1. The results presented for this deliverable (D2.1) include two generic configurations with the physical behavior of the system characterized by the dimensionless similarity Re numbers of 100 and 500, defined using the channel half-height. The two-dimensional geometry has the shape of a rectangular box Ω in which the S-like geometry is realized based on the immersed-boundary method [12] as a penalization domain. To this end, the rectangle has a total length of 1 [m], while the height is given by 0.2 [m]. The fluid domain (blue), defined by the wetted height $\delta = 0.05$ [m], is embedded in the larger rectangular box where the penalty approach implements the S-Bent geometry with a simple porosity term is used to penalize flow velocities and thereby represents the solid material (red), cf. Fig. 12. The corresponding flow is governed by the incompressible Navier-Stokes equation, viz.

$$\begin{aligned} \rho\frac{\partial\vec{v}}{\partial t} + \rho\left(\vec{v}\cdot\nabla\right)\vec{v} - \nabla\cdot\left(\mu\left(\nabla\vec{v} + \nabla\vec{v}^{\mathrm{T}}\right) + \nabla p + \beta\vec{v} = 0 \quad & \text{in } \Omega, \\ -\nabla\cdot\vec{v} = 0 \quad & \text{in } \Omega, \end{aligned} \tag{19}$$

where $\vec{\nabla}$ denotes the gradient operator, ρ [kg/m^3] is the density, ν [m^2/2] the fluid's viscosity, $\vec{v} = [u, v]^T$ [m/s] the velocity vector, p [m^2/s^2] the pressure, and β [1/s] the parameter defining the spatial porosity field.

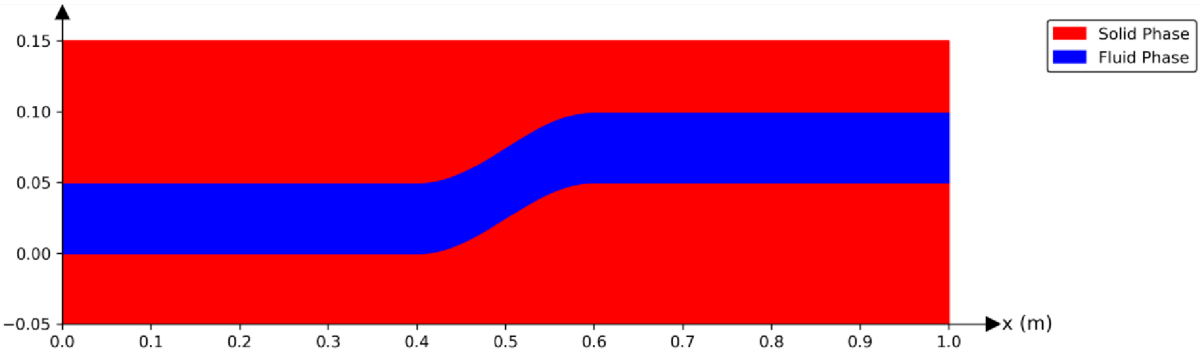

Figure 12: S-Bent case description, where the fluid (blue) and solid (red) mask dimensions are indicated.

The boundary conditions are set as follows. At the inlet, velocity is prescribed as $u(x) = u(z) = 0$, and a parabolic profile $u(y) = V_{\mathrm{ref}}\left(1 - (2(y - y_c)/H)^2\right)$ [m/s], with the reference velocity $V_{\mathrm{ref}} = 1$ [m/s], the channel height $H = 0.05$ [m], and the channel centerline $Y_c = 0.025$. The outlet flow velocity

This project receives funding from the European Union's Horizon 2020 HORIZON Research and Innovation Actions Programme under Grant Agreement #101080085

is defined as homogeneous Neumann with $\frac{\partial u}{\partial n} = 0$. The use of the penalization method is equivalent to no-slip boundary conditions on the velocity along the lower S-shaped outer walls. This implies a Neumann homogeneous for the pressure as it is implicitly prescribed by the momentum equation. In the case of the pressure, inlet and outlet conditions are set to homogeneous as $\frac{\partial p}{\partial n} = 0$ and zero, respectively. The initial conditions are set to zero for all velocity components and the pressure. The material properties ($\rho = 1$ [kg/m^3] for the incompressible assumption, $\nu = 5.0 \times 10^{-4}$ ($Re = 100$) and $\nu = 1.0 \times 10^{-4}$ ($Re = 500$) [m^2/s]) are assumed to remain constant over time. The configuration shown in this Figure has $\partial u/\partial n = \partial p/\partial n = 0$ for the outer upper and lower boundaries of the box. Table 6 summarizes all the boundary configurations. The spatial and temporal domains are discretized using the

Table 6: S-Bent boundary conditions.

boundary conditions	velocity	pressure
Top	$\frac{\partial u}{\partial n} = 0$	$\frac{\partial p}{\partial n} = 0$
Bottom	$\frac{\partial u}{\partial n} = 0$	$\frac{\partial p}{\partial n} = 0$
Left	(0 0 0)	$\frac{\partial p}{\partial n} = 0$
Right	$\frac{\partial u}{\partial n} = 0$	0
Inlet	u(y)	$\frac{\partial p}{\partial n} = 0$
Outlet	$\frac{\partial u}{\partial n} = 0$	0

finite volume method toolbox HELYX® (based on OpenFOAM® libraries) employing a cell-centered discretization. The integrals arising in the FV formulation are approximated using a second-order accurate midpoint rule. Diffusive fluxes are evaluated with a second-order central scheme, while convective fluxes are computed using a bounded second-order upwind scheme based on velocity gradients. The pressure-velocity coupling is handled using the PIMPLE algorithm.

The total number of simulated cases contain twelve different examples composed by two Re numbers (100 and 500), two $\beta = (1/\Delta t + 1/(\Delta x^2)\,\nu)\,\eta$ [1/s] parameters to implement the solid mask with $\eta = 0.03$ and 0.1 [-], and three meshes to evaluate the grid sensitivity.

All the flow configurations are solved on uniform structured grids that discretize the fluid and the solid domains homogeneously. A discretization study was carried out using three levels of refinement: coarse ($33,924$ cells), medium ($527,364$ cells), and fine ($2,103,300$ cells). The coarse grid resolves the solid domain with approximately $25,443$ cells, using a spacing of $\Delta x = 0.00195$ and $\Delta y = 0.0031$. Accordingly, the fluid domain is formed with approximately $8,481$ cells. For the medium grid, the cell size is set to $\Delta x = 0.000976$ and $\Delta y = 0.00155$. This configuration includes approximately $395,523$ (solid) and $13,1841$ (fluid) cells in the rectangular box. Finally, the fine grid increases the resolution to $525,825$ fluid cells and $1,577,475$ solid cells, with base cell sizes of $\Delta x = 0.000488$ and $\Delta y = 0.000778$. An overview of all three grid configurations is provided in Fig. 13.

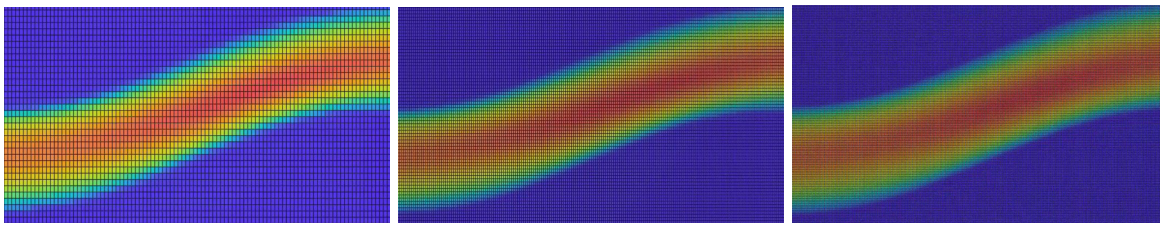

Figure 13: Representation of the discretization employed for the S-Bent case, for coarse (left), medium (middle) and fine (right) spatial meshes.

The visualization of Figure 14 exemplifies the velocity magnitude field for the finest grid and $Re = 100$. To assess discretization convergence, the total pressure loss along the channel centerline is examined. The corresponding results, presented in Table 7, demonstrate that the solution is effectively independent of the mesh resolution. For each of the twelve combinations Re number, β, and grid resolution, the steady-state velocity and pressure fields, along with the corresponding mesh, are available via DOI: doi.org/10.25592/uhhfdm.18561.

This project receives funding from the European Union's Horizon 2020 HORIZON Research and Innovation Actions Programme under Grant Agreement #101080085

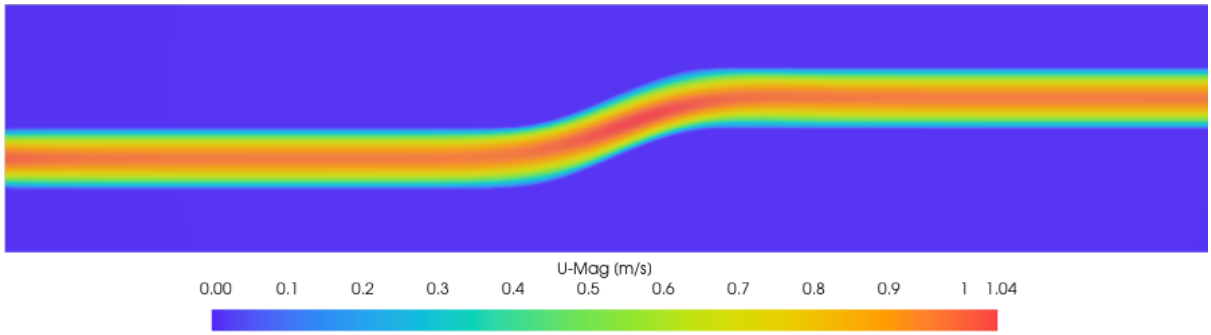

Figure 14: Velocity magnitude for the finest grid, $Re = 100$, and $\beta = 1405$ [1/s].

Table 7: Pressure loss for $Re = 100$ (left) and $Re = 500$(right).

	Δt [s]	p_{loss} [m^2/s^2]
Coarse	3.3352e-4	1.2934
Medium	1.6708e-4	1.3776
Fine	8.3624e-5	1.4916

	Δt [s]	p_{loss} [m^2/s^2]
Coarse	3.3352e-4	0.2720
Medium	1.6708e-4	0.2823
Fine	8.3624e-5	0.3072

A more realistic, industry-relevant application—such as a BEV cooling example is presented in Section 3.3.1.

3.2.7 Rayleigh-Bénard Convection – A Buoyancy Flow Experiment in 2D

This Rayleigh-Bénard convection (RBC) experiment addresses a two-dimensional scenario for buoyancy-driven flows. The experiment is characterized by a fluid layer subjected to heating from below $\tilde{T}_{\text{Hot}}\,[K]$ and cooling $\tilde{T}_{\text{Cold}}\,[K]$ from above at a constant Prandtl number of $Pr = 7.1$. A specific interest lies in the nonlinear interaction between the fluid's velocity and temperature, which gets increasingly difficult to resolve for very high Rayleigh numbers (Ra). The dynamics within the fluid with density $\tilde{\rho}\,[kg/m^3]$ and dynamic viscosity $\tilde{\mu}\,[kg/ms]$ are governed by the incompressible Navier-Stokes equations, which are closed using a Boussinesq approximation, treating density variations only within the buoyancy term.

For the sake of generalization, dimensions are omitted, and dimensional quantities, marked with a tilde, are transformed. To this end, the mean temperature $\bar{\tilde{T}} = (\tilde{T}_{\text{Hot}} + \tilde{T}_{\text{Cold}})/2\,[K]$ and the temperature difference $\Delta\tilde{T} = \tilde{T}_{\text{Hot}} - \tilde{T}_{\text{Cold}}\,[K]$ are defined. Furthermore, dimensionless quantities are defined through the Rayleigh number $Ra = \frac{\tilde{g}\tilde{\beta}\Delta\tilde{T}\tilde{L}^3}{\tilde{\nu}\tilde{\kappa}}$, which quantifies the ratio of buoyancy to dissipative effects and where $\tilde{g}\,[m/s^2]$ denotes gravitational acceleration, $\tilde{\beta}\,[1/K]$ the thermal expansion coefficient, $\tilde{\nu} = \tilde{\mu}/\tilde{\rho}$ the kinematic viscosity, $\tilde{L}\,[m]$ the characteristic length and $\tilde{\kappa}$ the thermal diffusivity. Introducing the Prandtl number $Pr = \tilde{\nu}/\tilde{\kappa}$, allow to link the Rayleigh and Reynolds numbers as $Re^2 = Ra/Pr$. Employing a free-fall scaling framework [13], the characteristic length scale is assumed as the cell height $\tilde{L}\,[m]$, such that the free-fall velocity is $\tilde{U}_{FF} = \sqrt{\tilde{g}\tilde{\beta}\Delta\tilde{T}\tilde{L}}$. This scaling naturally introduces the characteristic free-fall time scale $\tilde{t}_{FF} = \tilde{L}/\tilde{U}_{FF}$. Accordingly, the dimensionless velocity is $u = \tilde{u}/\tilde{U}_{FF}$. The temporal dimension transforms similarly to $t = \tilde{t}/\tilde{t}_{FF}$ such that a dimensionless time increment is $\Delta t = \Delta\tilde{t}/\tilde{t}_{FF}$. In this regard, the dimensionless governing equations for Rayleigh-Bénard convection can be expressed using the Einstein sum convention as

$$\begin{aligned} \frac{\partial}{\partial t}u_i + u_j\frac{\partial}{\partial x_j}u_i &= -\frac{\partial}{\partial x_i}p + \frac{1}{Re}\frac{\partial^2}{\partial x_i^2}u_i + \frac{Ra}{Pr\,Re^2}\theta\,\delta_{ij}\,, \\ \frac{\partial}{\partial t}\theta + u_j\frac{\partial}{\partial x_j}\theta &= \frac{1}{Re\,Pr}\frac{\partial^2}{\partial x_j^2}\theta\,, \\ \frac{\partial}{\partial x_j}u_j &= 0\,, \end{aligned} \tag{20}$$

where u_i denotes the i-th component of the non-dimensional velocity field in the two-dimensional problem, with $u_1 = u_x = u$ and $u_2 = u_y = v$. The variable p represents the non-dimensional kinematic

This project receives funding from the European Union's Horizon 2020 HORIZON Research and Innovation Actions Programme under Grant Agreement #101080085

Table 8: Geometrical and physical parameters for the study.

g	Pr	μ	ρ	L	T_{Hot}	T_{Cold}	$T_0 = \bar{T}$
$1\,[m/s^2]$	7.1	$0.00071\,[ks/ms]$	$1\,[kg/m^3]$	$1\,[m]$	$278.15\,[K]$	$268.15\,[K]$	$273.15\,[K]$

pressure, and $\theta = (\tilde{T} + \bar{\tilde{T}})/\Delta\tilde{T}$ corresponds to the dimensionless temperature. A turbulence model is not applied, and all discretized scales are resolved.

Periodic boundary conditions are imposed horizontally in the x-direction, along a domain of dimensionless width $H = \Gamma L$, with the aspect ratio $\Gamma = 2$. At the top and bottom plates, located at $\pm L/2$ from the centerline, Dirichlet no-slip boundary conditions are enforced for the velocity field ($u = v = 0$). Similarly isothermal Dirichlet conditions for the temperature $\theta(x, y = \pm L/2) = \pm\Delta T/2$ are prescribed. In the z-direction, the equations are not solved, and therefore, no boundary conditions are prescribed.

For the present experiment, a progressive study of increasing Rayleigh numbers, starting from $Ra = 10^8$, was conducted. Mesh resolutions were correspondingly refined to capture the increasingly finer flow scales inherent to higher Rayleigh number regimes, thereby ensuring sufficient resolution of all relevant fluid dynamic structures. To this end, simulations were performed on discretizations of 512×256 cells for $Ra = 10^8$ and 1024×512 cells for $Ra = 10^9$. In the z-direction, one single cell is used, rendering the problem effectively two-dimensional. The mesh consists exclusively of isotropic hexahedral cells, such that the grid spacings satisfy $\Delta x = \Delta y = \Delta z$. The computational domain is rectangular with an aspect ratio of 2:1. The FV method is employed for spatial discretization. All flow variables are stored at cell-centered locations, and the spatial grid is uniformly spaced in both directions. The simulations are conducted using the QCFD project partner's CFD platform HELYX®, which provides the necessary numerical algorithms and solvers. The pressure-velocity coupling is handled using the PIMPLE algorithm.

The geometrical and physical parameters used for the numerical study are summarized in Table 8. The $Ra = 10^8$ case is run with a dimensionless time step of 2.0×10^{-3} for $60,000$ iterations, terminating at a final dimensionless time of approximately 117.19. For the Rayleigh number of $Ra = 10^9$, a final dimensionless time of about 29.3 is reached by $30,000$ iterations with a dimensionless time step of 9.8×10^{-4}. Throughout all simulations, the temperature difference ΔT is kept constant and only $\tilde{\beta}$ is adjusted for setting the specific Rayleigh number. Non-dimensional key parameters are listed in Tab. 9. The instantaneous streamlines along contours indicating the velocity magnitude $|u|$ and temperature contours for both experiments are given in Figs. 15 and 16.

Table 9: Dimensionless characteristic parameters for different Rayleigh numbers.

Ra	Re	$\tilde{U}_{ff}$ [m/s]	$\tilde{t}_{ff}$[s]	$\tilde{\beta}$ [1/K]	Ra	Re	$\tilde{U}_{ff}$ [m/s]	$\tilde{t}_{ff}$[s]	$\tilde{\beta}$ [1/K]
10^8	$3,752.93$	2.665	0.3753	0.71	10^9	$11,867.82$	8.426	0.118 679	7.1

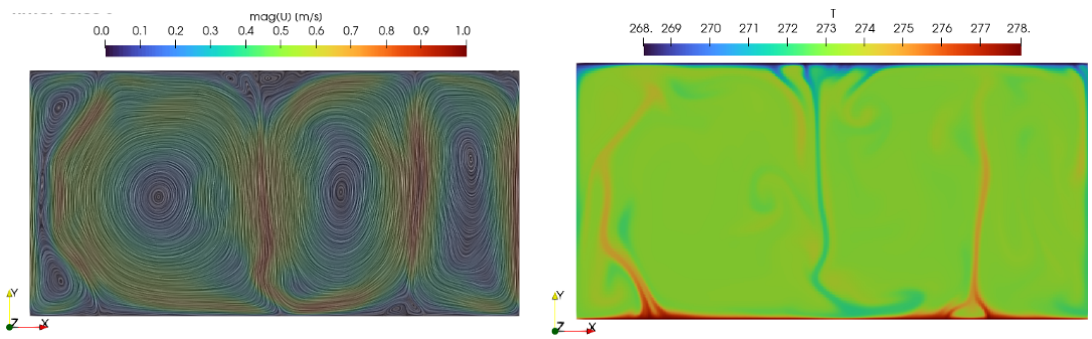

Figure 15: Instantaneous streamlines along contours indicating the velocity magnitude $|u|$(left) and temperature contours (right) for $Ra = 10^8$ at $\tilde{t} = 50\,[s]$.

This project receives funding from the European Union's Horizon 2020 HORIZON Research and Innovation Actions Programme under Grant Agreement #101080085

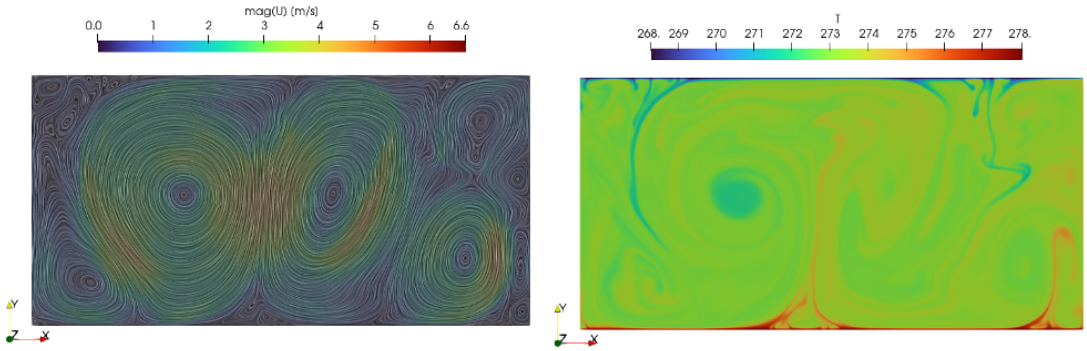

Figure 16: Instantaneous streamlines along contours indicating the velocity magnitude $|u|$ (left) and temperature contours (right) for $Ra = 10^9$ at $\tilde{t} = 4\,[s]$.

For the assessment of both cases, the instantaneous Nusselt number is defined as $Nu_{\text{inst}}(t) = 1 + \sqrt{Ra/Pr}\,\langle v(t), \theta(t)\rangle_V$, where $\langle\cdot\rangle_V$ denotes the spatial average over the entire computational domain. To characterize statistically stationary heat transfer, the time-averaged Nusselt number over a time window t_W is computed as

$$Nu(t_w) = \frac{1}{t_W}\int_{t_0}^{t_0+t_W} Nu_{\text{inst}}(t)\,dt, \tag{21}$$

with the initial time t_0 chosen to exclude initial transient effects. The two experiments are accordingly assessed, taking $t_0 = 50$ and $t_0 = 16.85$ respectively, such that the $Ra = 10^8$ case recovers $Nu(t_w) = 31.26$ and $Ra = 10^9$ results in $Nu(t_w) = 59$. For completeness, the temporal behavior is depicted in Figure 17, and the dashed lines show the temporal Nusselt average as well as the temporal offset t_0.

The benchmark is part of Ref. [14] and the datasets are again available for public open access via DOI: doi.org/10.25592/uhhfdm.18557.

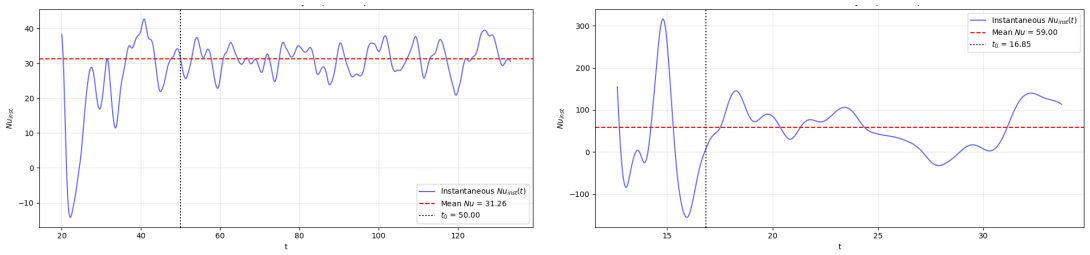

Figure 17: Instantaneous Nusselt number evolution for $Ra = 10^8$ (left) and $Ra = 10^9$ (right).

3.3 3D Applications

The final applications selected by the QCFD consortium for future comparisons with quantum methods focuses on the three-dimensional battery-pack cooling configuration. The complexity of this benchmark is deliberately designed to meet industrial requirements that are not yet achievable with current quantum CFD methods and available quantum hardware, but could be simulated on quantum computers in the near future using the aforementioned test cases for validation. Table 10 summarizes this three-dimensional test case, outlining its key characteristics and primary simulation objectives.

The objectives include: (1) the simulation of turbulent flows; (2) turbulence modeling using two-equation Reynolds-averaged Navier–Stokes (RANS) models; (3) the use of non-isotropic and non-homogeneous meshes; and (4) the analysis of complex internal flows with industrial relevance. The underlying physical processes are governed by steady (s) convection–diffusion equations (CD) and the conjugate heat transfer (CH), based on the Navier–Stokes equations (NSEs).

This project receives funding from the European Union's Horizon 2020 HORIZON Research and Innovation Actions Programme under Grant Agreement #101080085

Table 10: Summary of selected 3D cases.

3D Cases	Eqn.	Spatial	Temporal	#Eqn.	non/linear	Flow	#Grids	Num.	Focus	Ind.Relev.
Cooling of BEV	sCD/CH	3D	steady	3	non-linear	laminar/turbulent	3	FV	1,2,3,4	100%

3.3.1 Battery Electric Vehicle Cooling Case

The final case presented in D2.1 addresses a problem of particular relevance to BEVs and the automotive industry, namely the thermal management of a battery pack. In this context, the following scenario considers the fluid dynamic (momentum) behavior and the conjugate heat transfer within the cooling device of a battery pack thermal management system, as illustrated in Figure 18.

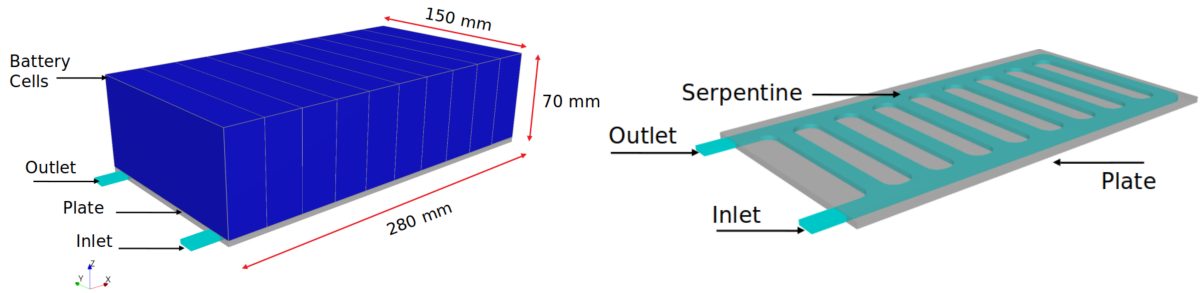

Figure 18: Case description of the BEV cooling system.

In particular, the investigated model represents a simplified 10-cell battery pack, where each cell generates a constant heat load of 1 [W]. The present study extends previously reported coolant-only serpentine benchmark cases documented in D1.1 [1] by incorporating solid regions and fully coupled thermal effects. A mesh sensitivity analysis was conducted using three levels of spatial resolution (coarse, medium, and fine) and two coolant flow regimes: laminar flow conditions ($Re \approx 560$), and turbulent flow conditions ($Re \approx 11,240$) modeled using a Reynolds-Averaged Navier–Stokes (RANS) approach in combination with a $k-\omega$ SST turbulence model and a default tabulated wall-function. The simulations are conducted using the QCFD project partner's openfoam-based CFD platform HELYX®, which provides the necessary numerical algorithms and solvers. They employ standard numerical algorithms for conjugate heat transfer analysis. The methodology and key results are summarized in the following.

The investigated system represents a simplified battery pack thermal management configuration consisting of multiple coupled physical regions. The model includes a coolant channel (water, 3 [mm] thickness), a cold plate (aluminum, 4 [mm] thickness), and a battery pack composed of 10 cells. Table 11 summarizes the material properties employed within the case. Each battery cell generates 1 [W] of heat uniformly, resulting in a total heat load of 10 [W]. The small gaps between adjacent battery cells are not explicitly resolved; instead, their thermal effect is represented using a thermal resistance layer $R_{\text{Layer}} = L/(\lambda\, A)$ [K/W], where A is the interface area, λ [W/(m K)] the thermal conductivity, and L [m] the layer thickness. All external boundaries are assumed to be thermally insulated using adiabatic conditions, implying no heat exchange with the surrounding environment.

Table 11: Material properties.

	ρ [kg/m^3]	λ [W/(m K)]	c_p [J/(kg K)]	μ [Pa s]
Cell	2,000	1	837	-
Coolant (water)	966.57	0.606	4,180	8.53×10^{-4}
Plate	2,700	237	902	-

The simulations are performed using a steady-state formulation with a segregated solver approach where the pressure–velocity coupling is handled via the SIMPLEC algorithm. The initial conditions are defined as the solid temperature $T_{\text{solid}} = 300$ [K] and the coolant temperature $T_{\text{coolant}} = T_{\text{inlet}} = 287.15$ [K], while the velocity and pressure fields are initialized using a potential flow solution. The channel walls

This project receives funding from the European Union's Horizon 2020 HORIZON Research and Innovation Actions Programme under Grant Agreement #101080085

are set to no-slip. The inlet flow conditions are selected as to $U = 0.1$ [m/s] ($Re \approx 560$; based on U, the hydraulic diameter of the coolant channel $h = 4.8$ [mm] and $\nu = 8.56 \times 10^{-7}$ [m/s^2]) and $U = 2$ [m/s] ($Re \approx 11,240$) for the streamwise velocity with a temperature of 287.15 [K] and homogeneous Neumann conditions for the pressure. The simulations are advanced until key monitored quantities, such as the pressure loss Δp or the maximum temperature at a given battery cell converge. For the laminar case, this takes approximately 200 iterations, while for the turbulent case it requires approximately $2,000$ iterations. Additionally, the integral quantities (Δp and $T_{\max}$) are additionally averaged over the final 500 iterations.

The mesh strategy is based on an anisotropic block mesh configuration to control the overall cell distribution. The domain is divided into two stacked blocks: (1) upper block (battery cell region) and (2) lower block (cold plate and coolant regions), viz. Figure 19. The initial discretization for the upper block is formed with cell sizes of coarse: $\Delta x = \Delta y = \Delta z = 4$ [mm], medium: $\Delta x = \Delta y = \Delta z = 2.8$ [mm], fine: $\Delta x = \Delta y = \Delta z = 2$ [mm]. The lower block for $\Delta x = \Delta y$ matches the corresponding upper block resolution, and $\Delta z = 2$ [mm] is selected for all meshes. Surface proximity refinement and local volumetric refinement are applied to increase resolution in the plate and coolant regions, with particular attention to resolving the thin 0.5 [mm] gaps between the plate and coolant. After the refinement, the final mesh resolutions in the lower block results is $\Delta x = \Delta y = 1$ [mm], $\Delta z = 0.5$ [mm] (coarse), $\Delta x = \Delta y = 0.7$ [mm], $\Delta z = 0.5$ [mm] (medium), and $\Delta x = \Delta y = 0.5$ [mm], $\Delta z = 0.5$ [mm] (fine). The overall mesh sizes are 2.1 million cells for the coarse, 4.2 million cells in the medium, and 8.3 million cells in the fine mesh. The coolant region is resolved using three boundary layers, achieving more than 99% layer coverage. Furthermore, an expansion ratio of 1.25 is used to ensure smooth growth from the wall region to the core flow.

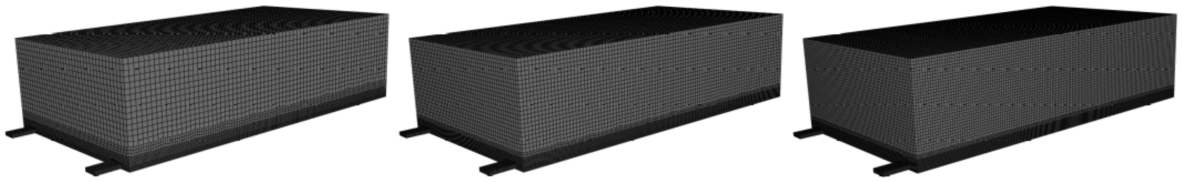

Figure 19: Coarse, medium, and fine meshes for the battery cells, the cold plate, and the coolant region.

The mesh sensitivity study is summarized in Table 12. These results show only minor differences in the key quantities between grid levels, indicating limited grid dependence and satisfactory numerical convergence. As expected, the laminar case ($Re \approx 560$) results in weaker convective heat transfer, leading to higher temperatures, particularly in downstream cells. Figure 20 indicates the maximum temperature at cell 10, reaching approximately 300.44 [K]. In contrast, the turbulent case ($Re \approx 11,240$) provides significantly enhanced cooling due to stronger convective transport, as observed in Figure 21. This results in lower peak temperatures and a more uniform temperature distribution across the battery pack, with a maximum temperature of approximately 296.35 [m] at cell 10. Consequently, the temperature difference between the hottest cell (cell 10) and the coolest cell (cell 1) is reduced from 4.2 [K] in the laminar case to 0.6 [K] in the turbulent case.

		Coolant		Plate	Cells
	Meshes	Δp [Pa]	T_{out} [K]	$T_{\max}$ [K]	$T_{\max}$ [K]
Laminar	Cell	30.16	287.82	292.492	300.435
	Coolant (water)	29.57	287.82	292.600	300.547
	Plate	29.26	287.82	292.681	300.630
Turbulent	Cell	3019	287.184	288.091	296.249
	Coolant (water)	3074	287.184	288.362	296.474
	Plate	3103	287.184	288.179	296.330

Table 12: Convergence results for the key metrics pressure loss and maximum temperature.

All the cases along with the corresponding meshes can be found via DOI: doi.org/10.25592/uhhfdm.18559.

This project receives funding from the European Union's Horizon 2020 HORIZON Research and Innovation Actions Programme under Grant Agreement #101080085

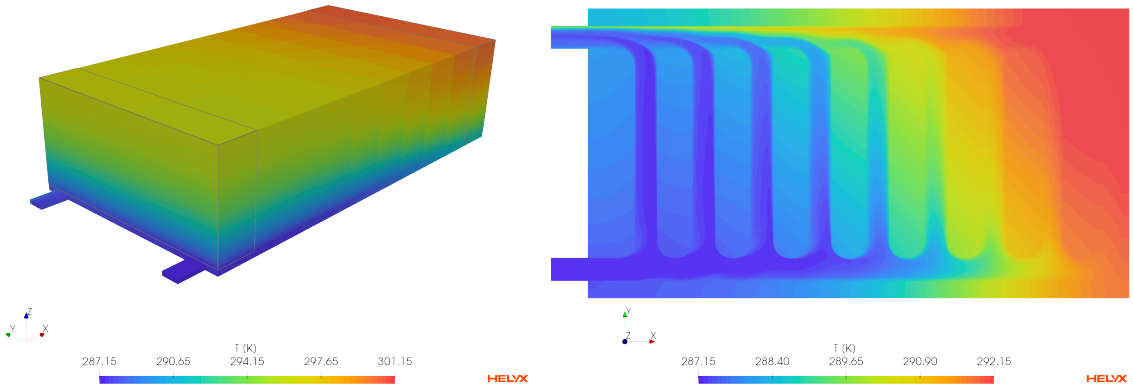

Figure 20: Temperature distribution for the fine mesh on the whole BEV cooling system. Flow in laminar conditions ($Re \approx 560$).

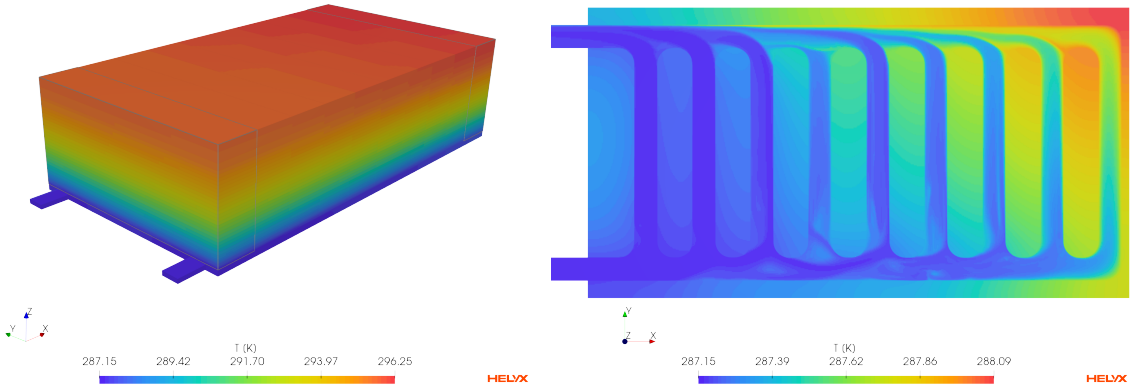

Figure 21: Temperature distribution for the fine mesh on the whole BEV cooling system using turbulent flow conditions ($Re \approx 11,240$).

References

[1] Quantum Computational Fluid Dynamics Consortium. Quantum Computational Fluid Dynamics – Core Benchmark CFD Set – Deliverable D1.1. Technical report, TUHH, UHH, ENGYS, FZJ, planqc, ENGYS, TUM, TUC, 2024.

[2] Sergio Bengoechea, Paul Over, Dieter Jaksch, and Thomas Rung. Toward variational quantum algorithms for generalized linear and nonlinear transport phenomena. *AIAA Journal*, 64(2):585–604, 2026.

[3] Paul Over, Sergio Bengoechea, Thomas Rung, Francesco Clerici, Leonardo Scandurra, Eugene de Villiers, and Dieter Jaksch. Boundary treatment for variational quantum simulations of partial differential equations on quantum computers. *Computers & Fluids*, 288:106508, 2025.

[4] Dieter Jaksch, Peyman Givi, Andrew J. Daley, and Thomas Rung. Variational quantum algorithms for computational fluid dynamics. *AIAA Journal*, 61(5):1885–1894, 2023.

[5] Michael Lubasch, Jaewoo Joo, Pierre Moinier, Martin Kiffner, and Dieter Jaksch. Variational quantum algorithms for nonlinear problems. *Physical Review A*, 101(1), Jan 2020.

[6] Paul Over, Sergio Bengoechea, Peter Brearley, Sylvain Laizet, and Thomas Rung. Quantum algorithm for the advection-diffusion equation by direct block encoding of the time-marching operator. *Phys. Rev. A*, 112:L010401, 2025.

This project receives funding from the European Union's Horizon 2020 HORIZON Research and Innovation Actions Programme under Grant Agreement #101080085

[7] Sergio Bengoechea, Paul Over, and Thomas Rung. Quantum time-marching algorithms for solving linear transport problems including boundary conditions. *International Journal for Numerical Methods in Engineering*, 127(8):e70326, 2026.

[8] Nis-Luca Van Hülst, Pia Siegl, Paul Over, Sergio Bengoechea, Tomohiro Hashizume, Mario Guillaume Cecile, Thomas Rung, and Dieter Jaksch. Quantum-inspired tensor-network fractional-step method for incompressible flow in curvilinear coordinates. *Computer Physics Communications*, page 110169, 2026.

[9] Joel H. Ferziger, Milovan Perić, and Robert L. Street. *Computational Methods for Fluid Dynamics*. Springer International Publishing, 2020.

[10] William J. Gordon and Charles A. Hall. Construction of curvilinear co-ordinate systems and applications to mesh generation. *International Journal for Numerical Methods in Engineering*, 7(4):461–477, 1973.

[11] Alexandre Joel Chorin. Numerical solution of the Navier-Stokes equations. *Mathematics of Computation*, 22(104):745–762, 1968.

[12] Charles S Peskin. Flow patterns around heart valves: A numerical method. *Journal of Computational Physics*, 10(2):252–271, 1972.

[13] Guenter Ahlers, Siegfried Grossmann, and Detlef Lohse. Heat transfer and large scale dynamics in turbulent rayleigh-bénard convection. *Rev. Mod. Phys.*, 81:503–537, Apr 2009.

[14] Nis-Luca van Hülst, Mario Guillaume Cecile, Hai-Yen Van, Tomohiro Hashizume, Eugene de Villiers, and Dieter Jaksch. Quantum-inspired simulation of 2D turbulent rayleigh-bénard convection, 2026.

This project receives funding from the European Union's Horizon 2020 HORIZON Research and Innovation Actions Programme under Grant Agreement #101080085